This is an *Accepted Manuscript*, which has been through the Royal Society of Chemistry peer review process and has been accepted for publication.

Accepted Manuscripts are published online shortly after acceptance, before technical editing, formatting and proof reading. Using this free service, authors can make their results available to the community, in citable form, before we publish the edited article. We will replace this *Accepted Manuscript* with the edited and formatted *Advance Article* as soon as it is available.

You can find more information about *Accepted Manuscripts* in the **Information for Authors**.

Please note that technical editing may introduce minor changes to the text and/or graphics, which may alter content. The journal's standard **Terms & Conditions** and the **Ethical guidelines** still apply. In no event shall the Royal Society of Chemistry be held responsible for any errors or omissions in this *Accepted Manuscript* or any consequences arising from the use of any information it contains.

Energy & Environmental Science

ARTICLE TYPE

High-performance sandwiched-porous polybenzimidazole membrane with enhanced alkaline retention for anion exchange membrane fuel cells

L. Zeng, T.S. Zhao*, L. An, G. Zhao, X.H. Yan

Alkaline doped polybenzimidazole (PBI) has been commonly utilized as anion exchange membranes in anion exchange membrane fuel cells (AEMFCs) over the past decade.
10 **However, the progressive release of doped alkali during fuel cell operation is a challenging issue for this type of membrane. To address this issue, we propose and fabricate a sandwiched-porous PBI (sp-PBI) membrane. The porous structure of the membrane prepared by a pore-forming method renders**
15 **numerous interconnected macropores and sponge-like walls, which provide enhanced attraction between the doped alkali and the PBI skeleton. Via this approach, both the ionic conductivity and alkali retention of the membrane are substantially enhanced. Meanwhile, to evaluate the**
20 **performance of the membrane in a H$_2$/O$_2$ AEMFC, we develop a new nanocomposite, PBI-decorated reduced graphene oxide (rGO) as the supporting material and then deposit electrocatalysts on this nanocomposite. This new catalyst structure not only exhibits a superior electro-**
25 **catalytic activity toward the oxygen reduction reaction, but also facilitates the mass transportation in the catalyst layer. It is demonstrated that the use of this new PBI-based membrane electrode assembly with the membrane and catalyst in the fuel cell can reach a peak power density of 544 mW cm^{-2},**
30 **which is among the highest power densities reported for this type of fuel cell in the existing literature.**

Alkaline doped polybenzimidazole (PBI), with its high hydroxide ion conductivity and its excellent chemical stability in alkaline media, has been utilized as anion exchange membranes (AEMs)
35 in alkaline direct alcohol fuel cells (ADAFCs) with marked performance.[1-5] The conductivities of alkaline doped PBI membranes are highly dependent upon the concentration of doped electrolyte,[6] which is acceptable in ADAFCs due to the fact that an alkali can be added directly to liquid fuels. However, there are
40 several challenging issues in fabricating a membrane electrode assembly (MEA) with PBI for H$_2$/O$_2$ AEMFCs.

One major challenge that needs to be addressed is that the long-term operation of alkaline doped PBI membranes can be affected by the progressive release of doped alkali, resulting in
45 the decreased ionic conductivity. In fact, the doped alkali, which is combined with the PBI skeleton by a hydrogen bonding

network, will be gradually leak via water transportation during the operation conditions.[7] Improving the retention of doped alkali in the PBI skeleton is vital for the alkaline doped PBI membrane.
50 The incorporation of alkaline-stable inorganic additives (such as nanostructured layered double hydroxide aerogels) into PBI membranes is an effective approach to improve the alkali retention ability due to the hydrophilicity of the composite membranes will be improved. However, this method was not
55 applied in alkaline doped PBI membrane because of the incompatibility between inorganic additives and PBI membranes.

Fabrication of the electrode with PBI as the binder is yet another challenge. PBI can only dissolve in polar solvents with high boiling points.[8-10] The solvents become very difficult to be
60 removed and are incompatible with the uniformly distributed catalysts, causing the agglomerates in the catalyst layer.[11, 12] Additionally, the dissolved PBI in solvents is a solution state, so that it can penetrated into all volumes in the catalyst layer during the preparation of catalyst layer, which blocks the transportation
65 of reactants to the electrochemical reactive sites.[10, 13] Thus, a strategic design of the catalyst layer with a well-established triple-phase-boundary (TPB) for ease of reactant/product, ion and electron transport is indispensable if PBI were to be used as the binder in catalyst layer.

70 To address the issues mentioned, in this work, we fabricate a sandwiched-porous PBI membrane (sp-PBI) and design a new catalyst structure using PBI-decorated reduced graphene oxide (rGO) as the supporting material. A schematic illustration is presented in Scheme 1. Porous PBI (p-PBI) fabricated by a pore-
75 forming method involves a large of interconnected macropores, which provide ample accessibility for the doped alkali as a result of the enhanced attraction between the PBI skeleton and the doped alkali. Thereafter, a dense PBI thin film was fabricated on either side of p-PBI to form the sp-PBI. A reduction of the
80 hydrogen permeability and improvement of the mechanical properties were achieved due to the sandwiched PBI dense layer in the sp-PBI, making it suitable for the application in H$_2$/O$_2$ AEMFCs. As for the electrode, a thin PBI layer was first introduced on the surface of graphene oxide (GO) through a
85 decorating process. The GO was subsequently reduced to reduced graphene oxide (rGO), forming the nanocomposites which are denoted as PBI/rGO. PBI located on the surface of rGO through π-π stacking interaction serves not only as binding sites for

anchoring the catalysts, but also as hydroxide-conducting pathways in the operation of H_2/O_2 AEMFCs. The catalysts, palladium nanowires (Pd NWs), were then deposited on the PBI/rGO surface. In this condition, we can simply disperse the catalyst into common solvents, such as isopropanol, to fabricate the catalyst layer without using high-boiling-point solvents. The catalysts were finally sprayed on the sp-PBI to form the MEA.

The novel MEA enables a H_2/O_2 AEMFC to operate at temperatures as high as 90°C with improved performance and stability. This result indicates that our strategy is a practical and effective approach to fabricate the PBI-based MEA for H_2/O_2 AEMFCs.
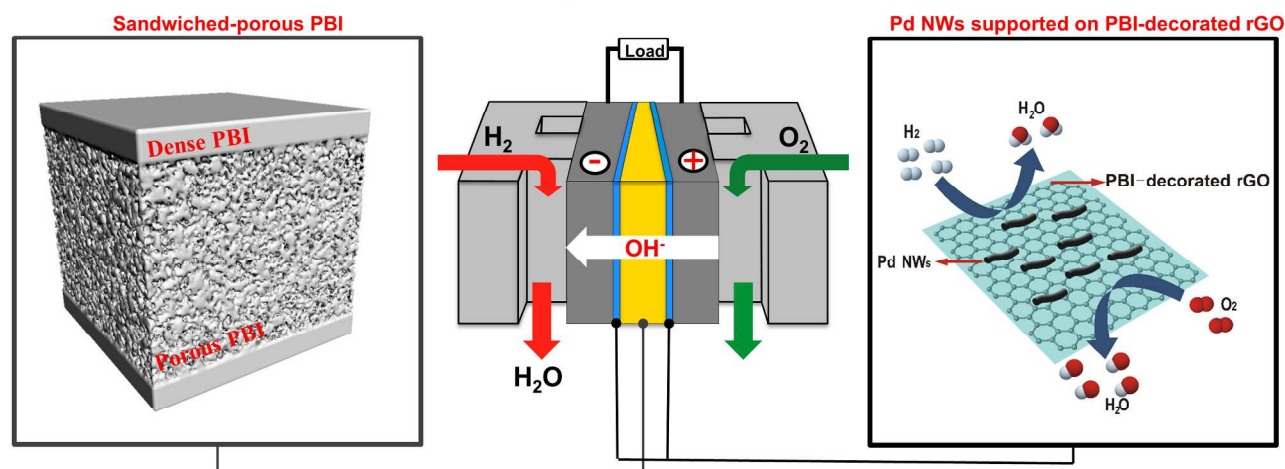
Scheme 1 Schematic illustration of a PBI-based membrane electrode assembly and the cell. The left side shows the sandwiched-porous PBI, while the right side shows Pd nanowires supported on PBI-decorated reduced graphene oxide and the electrochemical reaction on anode and cathode, respectively.
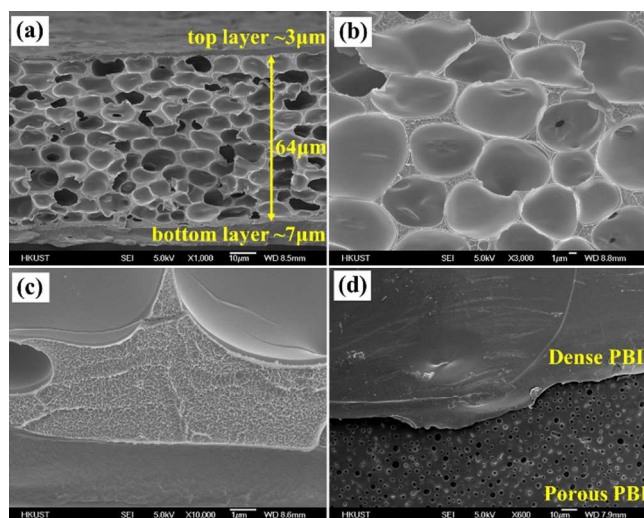

Fig. 1 SEM images of (a) low-revolution cross-sectional view of sp-PBI membrane; (b) porous PBI; (c) high-revolution of the porous and dense PBI; (d) surface morphology of sp-PBI membrane.

The p-PBI was fabricated by a pore-forming method with dibutyl phthalate (DBP) as the pore-forming additive. A dense PBI film was subsequently fabricated on either side of p-PBI to form the sp-PBI. A typical cross-sectional view of sp-PBI is presented in Fig. 1a, where the dense PBI film and porous PBI can be distinctly observed. The formation macropores with sponge-like walls are shown in Fig. 1b and Fig. 1c. The porosity of p-PBI could be controlled by simply varying the ratio between PBI and DBP (Table S1). The introduction of porous structure in the form of sponge-like walls could improve the uptake of the doped alkali, resulting from the enhanced capillary forces (Fig.

S1). From Fig. 1c, it is apparent that the dense PBI was in intimate contact with the porous PBI without the formation of voids, which would be favourable to the mass transportation (H_2O and hydroxide ions). Meanwhile, the surface pores in the p-PBI membrane with the pore sizes ranging from 1.2 μm to 4 μm were completely covered by the fabricated dense PBI (Fig. 1d). Undoubtedly, the fabrication of the dense PBI thin film will improve the alkali retention ability and reduce the gas permeability.
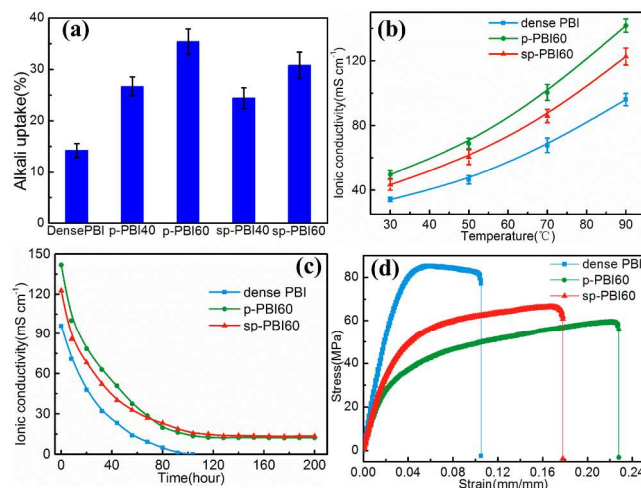

Fig. 2 Alkali uptake (a) and ionic conductivity (b) of different types of alkaline doped PBI (6 M KOH); (c) the durability test of ionic conductivity at 90°C; (d) The stress-strain curves of dense PBI, p-PBI60 and sp-PBI60.

To assess the ionic conductivity of this novel structure, we measured the alkali uptake and ionic conductivity of different

PBI membranes with the same thickness (~80 μm) (Fig. 2a). After being doped by 6 M KOH, an improvement in alkali uptake of p-PBI is observed with an increase in the porosity. For example, when the porosity reaches to 60%, the alkali uptake of

5 p-PBI (35.4%) is about 1.5-fold higher than that of dense PBI (14.2%). However, the alkali uptake of sp-PBI membranes decreases to some extent after the thin dense PBI film was fabricated on the surface of p-PBI. This is expected since porous structure in p-PBI has stronger capillary forces which abosrb

10 alkali, than that of the fabricated dense PBI film. Nevertheless, the alkali uptake of sp-PBI is much higher than that of dense PBI (30.8% for sp-PBI60 *vs.* 14.2% for dense PBI). The ionic conductivities of different types of PBI membranes were also measured at different temperatures (Fig. 2b). As expected, the

15 ioinc conductivities of p-PBI and sp-PBI are higher than that of dense PBI, particularly at elevated temperatures. For example, the ioinc conductivity of p-PBI with 60% porosity is 141.8 mS cm^{-1} at 90ºC, in comparison to 96.1 mS cm^{-1} for dense PBI. As the similar trend with alkali uptake, the ioinc conductivity of sp-PBI

20 reduces to 122.6 mS cm^{-1}, which is still 30% higher than that of dense PBI. The marked improvement in conductivity is ascribed to the enhanced attraction of the doped alkali on the porous stucture of p-PBI. The ioinc conductivities and the alkali uptakes of different types of PBI membranes were continuously measured

25 at 90ºC, as illustrated in Fig. 2c and Fig. S2, respectively. The ionic conductivity and the alkali uptake of dense PBI declines dramatically over time. After about 90 hours, the ionic conductivity of dense PBI reduces to almost zero as a result of the complete release of the doped alkali. While a decline in

30 conductivity is observed in both p-PBI and sp-PBI, especially at the initial stage, the rates of decline are lower than that of dense PBI (Fig. S3). It is testified that the enhanced capillary forces in the porous structure relieve the release of the doped alkali. More importantly, the final conductivities for both p-PBI and sp-PBI

35 kept at ~13 mS cm^{-1}, instead of reduction to zero. It is further demonstrated that the porous stuctures increase the alkali retention during the long-term operation.

The gas permeability and mechanical properties were also measured for these types of PBI membranes. The hydrogen

40 permeabilities at different temperatures are exhibited in Table S2. Without the alkaline doping process, both the dense PBI and the sp-PBI membrane exhibit a very low hydrogen permeability, which is in good agreement with the results reported in the literature.[14, 15] The low hydrogen permeability is also

45 demonstrated that the pores formed in the porous structure were completely covered by the dense PBI layer. After being doped with 6 M KOH, the polymer backbones of PBI membrane are separated by the doped alkali, thereby resulting in the facile diffusion of permeated hydrogen through alkaline doped PBI

50 membranes. The sp-PBI membrane shows a relatively larger hydrogen permeability than dense PBI due to the thickness of dense layer (i.e., sandwich skeleton) is thinner than that of the dense PBI. The stress-strain curves of dense PBI, p-PBI and sp-PBI were then measured. As exhibited in Fig. 2d, the introduction

55 of pores in p-PBI reduces the mechanical properties, including the tensile strength at break and Young's modulus (Table S3). However, after the fabrication with a thin PBI layer on both side of p-PBI, the mechanical properties are improved to some extent.

For example, the tensile strength at break of sp-PBI with 60%

60 porosity is 66.6 MPa, in comparison to 59.6 MPa for p-PBI with the same porosity. Although the mechanical properties of sp-PBI are lower than that of dense PBI, the mechanical properties reported here are still higher than that of AEMs reported in the literature and satisfy the requirement employing in AEMFCs.[16-18]

65 Furthermore, we designed a new catalyst structure using PBI-decorated rGO as the supporting material (Scheme 1). PBI/rGO was prepared through the reduction of GO in the presence of PBI. The structural and morphological properties of the hybrids were characterized by FTIR, TEM and atomic force

70 microscopy (AFM). In the FTIR spectrum of PBI/rGO (Fig. 3a), most of the peaks related to the oxygen-containing moieties in the pristine GO vanished, while the new peaks attributing to the C-N and N-H skeletal vibrations appeared during the reduction of GO in the presence of PBI. This result confirms that rGO is coated by

75 PBI thin film. A typical TEM image of as-synthesized PBI/rGO is shown in Fig. S4. PBI/rGO samples are crumpled and entangled with each other, resulting from an increased surface tension of the decorated PBI. Also, AFM was employed to measure the thickness of PBI/rGO and rGO, which was prepared

80 by the same reduction process in the absence of PBI (Fig. 3b and Fig. S5). Based on more than 50 individual measurements of different flat graphene nanosheets, the average thicknesses of rGO and PBI/rGO are 1.46 nm and 2.77 nm, respectively. Indisputably, the increase in thickness (1.31 nm) can be attributed

85 to the coverage of PBI on the rGO. On the other hand, we applied electrochemical impedance spectroscopy (EIS) to measure the resistance of rGO and PBI/rGO (Fig. S6). It is revealed that the resistance of PBI/rGO (19.8 mΩ) is only slightly higher than that of rGO (18.7 mΩ), indicating that the PBI/rGO preserves the

90 excellent electrical conductivity of graphene, which is an important requirement for materials used as supporting materials in the catalyst layer. On the basis of these characterizations, we successfully prepared the PBI/rGO supporting materials, which not only preserve the superior electrical property of graphene, but

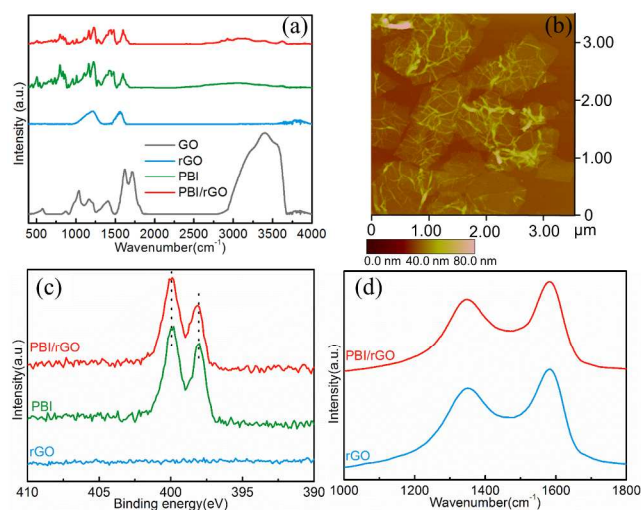95 also facilitate the hydroxide ion conduction, as will be discussed below.

Fig. 3 (a) FTIR spectra of the graphene oxide, graphene, PBI membrane and PBI-wrapped graphene; (b) a typical AFM micrograph of PBI/rGO;
100 (c) N 1s XPS spectra of rGO, pristine PBI and PBI/rGO; (d) Raman spectra of rGO and PBI/rGO.

It is suggested that PBI decorates the GO through the two interactions: (1) hydrogen bonding between the benzimidazole moiety of PBI and the hydroxyl and/or carbonyl groups of GO, created during the modified Hummers method; (2) π-π stacking interaction between the large π-conjugated structure of graphene and the benzimidazole moiety of PBI. The interaction of hydrogen bonding is reduced while the π-π stacking interaction is enhanced during the reduction of GO. Nevertheless, the strong interactions derived from the non-covalent bonds between the two materials can be favourable to the formation of a stable hybrid material in which the PBI uniformly decorates the surface of rGO. For the interaction between PBI and rGO, we used X-ray photoelectron spectroscopy (XPS) and Raman measurement to confirm this type of interaction, as presented in Figs. 3c-3d. The appearance of N 1s peaks in PBI/rGO verifies the decorating process as the peaks are derived from the PBI. The spectra of N 1s derived from the pristine PBI are also presented in Fig. 3c for comparison. The spectra of PBI/rGO in the N 1s region are split into two peaks, centering at 398.0 eV and 399.9 eV, respectively, due to the double-bonded and single-bonded nitrogen in the benzimidazole rings (Fig. S7).[19] After the decorating process, the binding energy of N 1s remains the same value despite an observable reduction in the peak intensity, indicating that the PBI is physically absorbed onto the rGO surface. The physical absorption can also be proven by Raman spectra. The G peak at 1582.96 cm^{-1}, which came from the rGO of PBI/rGO, remains somewhat unchanged in comparison to that of the pristine rGO where the G peak is located at 1584.45 cm^{-1} (Fig. 3d). Thus, these measurements demonstrate that PBI is absorbed on the surface of rGO through non-covalent π-π stacking interactions,[20, 21] and the intrinsic electronic and structural properties of graphene are preserved during the decorating process.
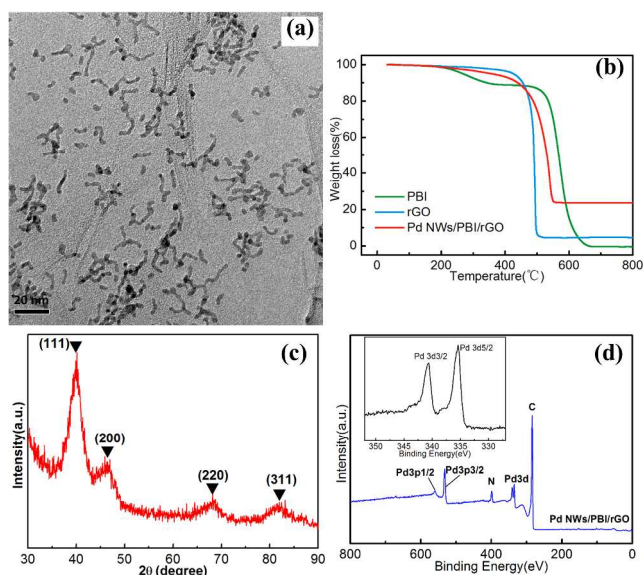

Fig. 4 (a) Typical TEM image of Pd NWs/PBI/rGO catalysts. (b) TGA curve of the Pd NWs/PBI/rGO. (c) XRD spectrum and (d) XPS spectrum of Pd NWs/PBI/rGO catalysts (inset: the Pd 3d region.).

To measure the properties of nanocomposites as the supporting materials, we synthesized the Pd NWs (Fig. S8), which were demonstrated with high electrocatalytic activities,[22, 23] and deposited Pd NWs on the surface of PBI/rGO to form the

catalysts. A typical TEM image of the electrocatalysts, denoted as Pd NWs/PBI/rGO, is presented in Fig. 4a. It is seen that Pd NWs are uniformly deposited on the surface of PBI/rGO. The Pd loading in Pd NWs/PBI/rGO revealed by inductively coupled plasma mass spectrometry (ICP-MS) is 23.1 wt.%, which is almost the same with the TGA data (23.5 wt.%) performed under the air atmosphere (Fig. 4b). The weight loss in Pd NWs/PBI/rGO at the temperature lower than 500°C attributes to the decorated PBI in the sample.[24, 25] The formation of Pd NWs/PBI/rGO catalysts was characterized by XRD as shown in Fig. 4c; all peaks can be indexed to the face centered cubic (*fcc*) crystalline palladium (JCPDS card No. 05-0681). The surface property of Pd NWs/PBI/rGO was also studied by XPS (Fig. 4d), exhibiting the Pd 3d and Pd 3p peaks together with a C 1s peak (284.0 eV) and an N 1s peak (399.0 eV). The content of N in the sample was 6.7 wt.%, indicating that the content of decorated PBI in the Pd NWs/PBI/rGO was 6.7 wt.%. A high-resolution Pd 3d spectrum is shown in the inset of Fig. 4d, where doublet peaks are located at 340.7 eV and 335.4 eV, which are attributed to Pd^0 3d3/2 and Pd^0 3d5/2, respectively.

The electrocatalytic activity of as-prepared Pd NWs/PBI/rGO was then determined by the oxygen reduction reaction (ORR) in the alkaline media. The electrocatalytic activity of catalysts was first evaluated by cyclic voltammetry (CV) and the result is presented in Fig. 5a. The integration of charges in the reduction of PdO to Pd in the potential range of +0.9 V to +0.5 V vs. RHE can be used to determine the electrochemical surface area (ECSA), assuming that the theoretical reduction charge of PbO monolayer is 405 μC cm^{-2}.[26, 27] Based on this evaluation, the ECSA of Pd NWs/PBI/rGO is 49.5 m^2 g^{-1}, indicating that the catalyst has a larger accessible ECSA. We also used AC impedance to measure the internal resistance of the glassy carbon electrode (GCE) which was deposited with Pd NWs/PBI/rGO and the physical mixture of Pd NWs and rGO in the three-electrode cell under otherwise identical preparation and test conditions. As shown in Fig. S9, the spectrum of the Pd NWs/PBI/G shows a slight increase in the high-frequency-region resistance, clarifying the good electrical communication between the Pd NWs and PBI/G.

To further investigate the ORR performance of Pd NWs/PBI/rGO, we performed rotating disk electrode (RDE) measurements in 0.1 M KOH solution saturated with oxygen. The related polarization curves of Pd NWs/PBI/rGO with the electrode rotation rate which varied from 200 rpm to 2000 rpm are displayed in Fig. 5b. The electron-transfer kinetics was evaluated by Koutecky-Levich analysis at different potentials. The electron-transfer number per oxygen molecule (*n*) in ORR is obtained to be about 4.0, demonstrating that Pd NWs/PBI/rGO favors a four-electron reduction process for ORR (Fig. 5c). The kinetic currents derived from the mass transport correction of total currents (Fig. 5d) show Tafel slope of 58.6 mV per decade and 103.7 mV per decade at low currents and high currents, respectively. The two segmentations with different slopes were widely observed in the ORR process, indicating that the coverage conditions of the reaction intermediate was changed.[28] The intrinsic kinetic current density at +0.9 V vs RHE, which is considered as a standard metric for evaluating the specific activities of ORR catalysts, is calculated and presented in Table

S4[29]. At +0.9 V, Pd NWs/PBI/rGO exhibits a specific activity of 0.54 mA cm_{Pd}^{-2} and a mass activity of 0.28 mA μg_{Pd}^{-1}, which is higher than that of previous Pd-based catalysts reported in the open literature.[26, 27, 30-33] The enhanced ORR activity is attributed to the peculiar wavy morphology of Pd NWs and the copious existence of twin defects, which were demonstrated with high electrocatalytic activity toward ORR in the alkaline media.[27, 34]
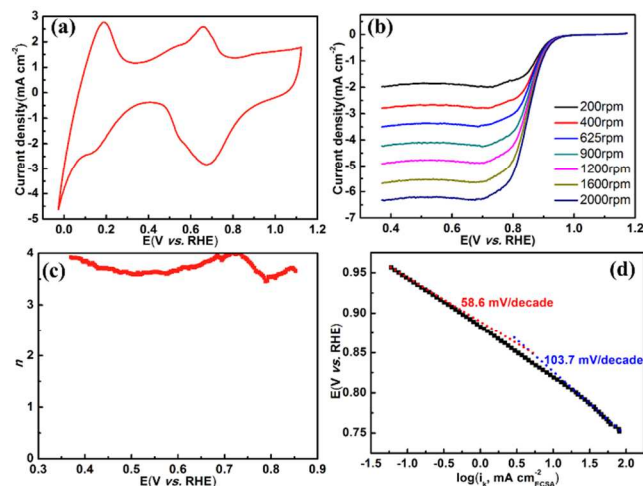

Fig. 5 (a) CV curve of Pd NWs/PBI/rGO catalysts in a N_2-saturated 0.1 M KOH. (b) LSV curves of Pd NWs/PBI/rGO catalysts in an O_2-saturated 0.1 M KOH with a sweep rate of 5 mV s^{-1} at different rotation rates. (c) Electron-transfer number calculated from LSV curves for Pd NWs/PBI/rGO catalyst. (d) Kinetic current densities versus potential derived from the mass transport correction of the corresponding disk currents in (b) at 1600 rpm.

Finally, we tested the cell performance and durability of a membrane electrode assembly (MEA), respectively employing Pd NWs/PBI/rGO and sp-PBI as the catalysts and membrane, denoted as novel MEA. For the purpose of comparison, a conventional MEA was fabricated with Pd NWs and the dense PBI membrane as the catalyst and membrane, respectively. In the conventional MEA, PBI solution (dissolved in DMAc) with a loading of 6.7 wt.% was added into the catalyst layer. The polarization and power density curves of H_2/O_2 AEMFCs at 90°C are presented in Fig. 6a. A high open circuit voltage (about 1.0 V) indicates that the decorated PBI does not affect the catalyst utilization.[11] The novel MEA exhibits a peak power density of 544.4 mW cm^{-2}, which is higher than the conventional MEA (396.8 mW cm^{-2}). In comparison, our novel PBI-based MEA outperforms the conventional state-of-the-art H_2/O_2 AEMFCs which use commercial ionomer/membrane (Tokuyama Corp.) at 80°C (500 mW cm^{-2})[35], the commercial ionomer (Acta. S.p.A.) at 50°C (~500 mW cm^{-2})[36], the polysulfone-based ionomer/membrane at 70°C (342 mW cm^{-2})[37] and the poly(2,6-dimethyl-1,4-phenyloxide)-based ionomer/ membrane (242 mW cm^{-2})[38]. The performance is also completive with the performance of the MEA reported in recent literature, which used the guanidinium functionalized perfluorinated polyphenylene as the membrane, yielding a peak power density of 577 mW cm^{-2} at 80°C.[39] This superior performance is explained as follows. As expected, the efficient TPB established due to the elaborate fabrication process of the catalyst layer builds a pathway for both the mass transportation and electron conduction. On the other

hand, Pd NWs with wavy morphologies have also been demonstrated to exhibit high electrocatalytic activity toward ORR in the three-electrode cell. Finally, sp-PBI is beneficial for the ionic conduction and the water transportation in the membrane, which reduce internal resistance of the MEA. The internal resistance was measured by AC impedance; the internal resistance of novel MEA is 0.294 Ω cm[2], which is lower than that of the conventional MEA (0.398 Ω cm[2]).
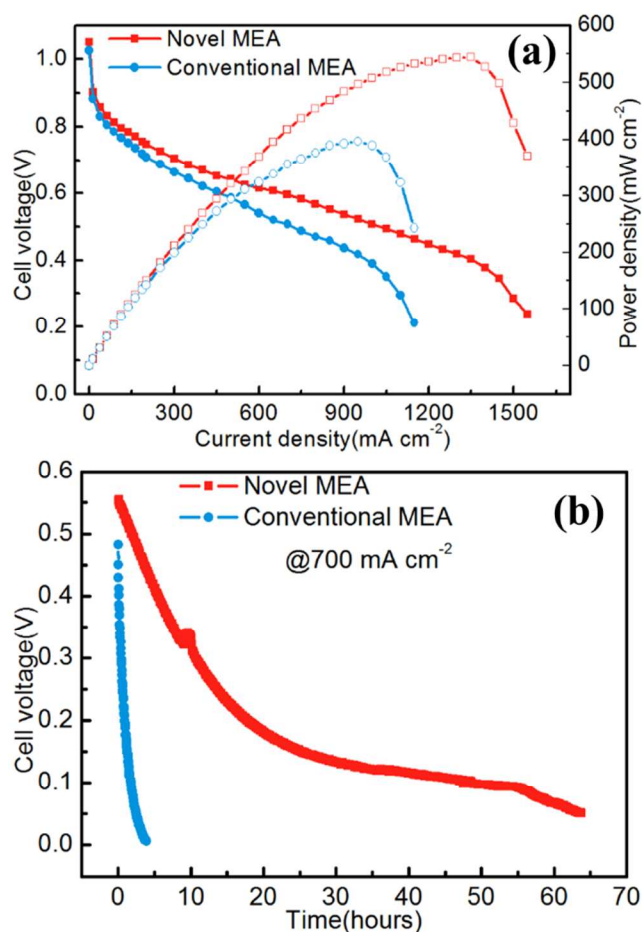

Fig. 6 (a) Polarization curves (filled symbols) and power-density curves (hollow symbols) of H_2/O_2 AEMFCs with conventional MEA (round symbols) and novel MEA (square symbols); (b) Constant current discharge of the H_2/O_2 AEMFC using conventional MEA and novel MEA with O_2 as the oxidant at a current density of 700 mA cm^{-2}. Operating conditions: cell temperature 90°C, humidifier temperatures 90°C for both H_2 and O_2, flow rate 300 mL min^{-1}, and back pressure 30 psi for both H_2 and O_2.

Fig. 6b shows the operating stability of the MEA with fully humidified oxygen as the oxidant. The measurement was performed at a constant current of 700 mA cm^{-2}. The conventional MEA showed a dramatic drop in voltage to almost zero over the course of 5 hours. The voltage drop is caused by a progressive release of the doped alkali from the dense PBI, thereby inhibiting the ionic conduction in the membrane. However, the novel MEA demonstrates improved stability when compared with the conventional MEA. The cell voltage gradually reduces from 0.55 V to around 0.1 V after 30 hours, and remains at this voltage for another 25 hours. The cell voltage reduces to zero after about 65 hours. This result can be attributed to the fact

that the sp-PBI membrane enables an improvement in the attraction of the doped alkali on the sponge-like wall structures, retarding the progressive release of the doped alkali during the constant current discharge. Meanwhile, due to the high efficient ionic conduction of sp-PBI, the generated ions (OH^-) at the cathode can effectively transfer from the cathode to anode, thereby mitigating the dependence of the ionic conductivity on the doped alkali in the sp-PBI membrane. Although the operating stability of novel MEA shows a marked improvement in comparison to that of the conventional MEA, the sponge-like structure is unable to completely prevent the release of the doped alkali. Hence, the cell voltage reduction is still observed over time, due to a gradual depletion of the doped alkali, but it should be noted that the novel MEA can be further discharged if it were doped with 6 M KOH again. Nevertheless, the novel PBI-based MEA is proposed for the first time and demonstrated with the enhanced power density and improved stability for H_2/O_2 AEMFCs, especially at elevated temperature.

In summary, a novel PBI-based MEA, with a sandwiched-porous PBI membrane and a new catalyst structure using PBI-decorated rGO as the supporting material, was fabricated for H_2/O_2 AEMFCs. The sp-PBI was prepared by a pore-forming method consisting of a large of interconnected macropores and sponge-like walls, which provided enhanced attraction between the doped alkali and the PBI skeleton. Hence, both the ionic conductivity and alkali retention ability were enhanced when compared with the dense PBI membrane. Furthermore, a novel catalyst supporting material, PBI/rGO, was fabricated. It was demonstrated that the superior electrical property of graphene was preserved during the decorating process. After being deposited with ultrathin Pd NWs, Pd NWs/PBI/rGO catalysts exhibited a high electrocatalytic activity toward ORR, resulting from the peculiar wavy structure and the copious existence of twin defects. When the as-prepared Pd NWs/PBI/rGO catalysts were applied to fabricate the catalyst layer, the triple phase boundary was readily established. Hence, the novel PBI-based MEA enabled a H_2/O_2 AEMFC to yield a peak power density of 544 mW cm^{-2} at 90°C. Moreover, the novel PBI-based MEA continuously discharged at a constant current of 700 mA cm^{-2} at 90°C with the improved stability compared with the conventional MEA. It is believed that this work will offer a new approach in fabricating the catalyst structure possessing a well-established triple phase boundary, and pave a way for the breakthroughs in the development of AEMFCs technology to achieve a superior cell performance.

Notes and references

a Department of Mechanical Engineering, The Hong Kong University of Science and Technology, Clear Water Bay, Kowloon, Hong Kong SAR, China. Fax: (852)23581543; Tel: (852) 23588647; E-mail: metzhao@ust.hk (T.S. Zhao)

1. J. R. Varcoe and R. C. T. Slade, *Fuel Cells*, 2005, **5**, 187-200.
2. H. Y. Hou, G. Q. Sun, R. H. He, Z. M. Wu and B. Y. Sun, *J Power Sources*, 2008, **182**, 95-99.
3. H. Y. Hou, G. Q. Sun, R. H. He, B. Y. Sun, W. Jin, H. Liu and Q. Xin, *Int J Hydrogen Energ*, 2008, **33**, 7172-7176.
4. A. D. Modestov, M. R. Tarasevich, A. Y. Leykin and V. Y. Filimonov, *J Power Sources*, 2009, **188**, 502-506.
5. L. An, T. S. Zhao, Y. S. Li and Q. X. Wu, *Energ Environ Sci*, 2012, **5**, 7536-7538.
6. B. Xing and O. Savadogo, *Electrochem Commun*, 2000, **2**, 697-702.
7. H. Y. Hou, S. L. Wang, Q. A. Jiang, W. Jin, L. H. Jiang and G. Q. Sun, *J Power Sources*, 2011, **196**, 3244-3248.
8. J. Lobato, P. Canizares, M. A. Rodrigo, J. J. Linares and G. Manjavacas, *J Membrane Sci*, 2006, **280**, 351-362.
9. A. A. Lysova, I. I. Ponomarev and A. B. Yaroslavtsev, *Solid State Ionics*, 2011, **188**, 132-134.
10. A. Su, Y. M. Ferng and X. Y. Tsai, *Int J Energ Res*, 2013, **37**, 1213-1222.
11. S. Gu, R. Cai, T. Luo, Z. W. Chen, M. W. Sun, Y. Liu, G. H. He and Y. S. Yan, *Angew Chem Int Edit*, 2009, **48**, 6499-6502.
12. J. Lobato, P. Canizares, M. A. Rodrigo, J. J. Linares and F. J. Pinar, *Int J Hydrogen Energ*, 2010, **35**, 1347-1355.
13. C. Wannek, W. Lehnert and J. Mergel, *J Power Sources*, 2009, **192**, 258-266.
14. R. H. He, Q. F. Li, A. Bach, J. O. Jensen and N. J. Bjerrum, *J Membrane Sci*, 2006, **277**, 38-45.
15. D. Aili, M. K. Hansen, R. F. Renzaho, Q. F. Li, E. Christensen, J. O. Jensen and N. J. Bjerrum, *J Membrane Sci*, 2013, **447**, 424-432.
16. N. J. Robertson, H. A. Kostalik, T. J. Clark, P. F. Mutolo, H. D. Abruna and G. W. Coates, *J Am Chem Soc*, 2010, **132**, 3400-3404.
17. T. J. Clark, N. J. Robertson, H. A. Kostalik, E. B. Lobkovsky, P. F. Mutolo, H. D. Abruna and G. W. Coates, *J Am Chem Soc*, 2009, **131**, 12888-+.
18. Y. G. Wu, C. M. Wu, F. Yu, T. W. Xu and Y. X. Fu, *J Membrane Sci*, 2008, **307**, 28-36.
19. M. Okamoto, T. Fujigaya and N. Nakashima, *Small*, 2009, **5**, 735-740.
20. S. Y. Wang, X. Wang and S. P. Jiang, *Phys Chem Chem Phys*, 2011, **13**, 7187-7195.
21. S. Zhang, Y. Y. Shao, H. G. Liao, M. H. Engelhard, G. P. Yin and Y. H. Lin, *Acs Nano*, 2011, **5**, 1785-1791.
22. Y. Wang, S. I. Choi, X. Zhao, S. F. Xie, H. C. Peng, M. F. Chi, C. Z. Huang and Y. N. Xia, *Adv Funct Mater*, 2014, **24**, 131-139.
23. E. Antolini, *Energ Environ Sci*, 2009, **2**, 915-931.
24. T. Fujigaya, T. Uchinoumi, K. Kaneko and N. Nakashima, *Chem Commun*, 2011, **47**, 6843-6845.
25. M. R. Berber, T. Fujigaya, K. Sasaki and N. Nakashima, *Sci Rep-Uk*, 2013, **3**.
26. L. Jiang, A. Hsu, D. Chu and R. Chen, *J Electrochem Soc*, 2009, **156**, B643-B649.
27. M. H. Seo, S. M. Choi, H. J. Kim and W. B. Kim, *Electrochem Commun*, 2011, **13**, 182-185.
28. N. M. Markovic, H. A. Gasteiger and P. N. Ross, *J Phys Chem-Us*, 1995, **99**, 3411-3415.
29. H. A. Gasteiger, S. S. Kocha, B. Sompalli and F. T. Wagner, *Appl Catal B-Environ*, 2005, **56**, 9-35.
30. W. Sun, A. Hsu and R. R. Chen, *J Power Sources*, 2011, **196**, 4491-4498.

31. S. Maheswari, P. Sridhar and S. Pitchumani, *Electrochem Commun*, 2013, **26**, 97-100.

32. K. Jukk, N. Alexeyeva, C. Johans, K. Kontturi and K. Tammeveski, *J Electroanal Chem*, 2012, **666**, 67-75.

33. G. T. Fu, X. Jiang, L. Tao, Y. Chen, J. Lin, Y. M. Zhou, Y. W. Tang and T. H. Lu, *Langmuir*, 2013, **29**, 4413-4420.

34. F. H. B. Lima, J. Zhang, M. H. Shao, K. Sasaki, M. B. Vukmirovic, E. A. Ticianelli and R. R. Adzic, *J Phys Chem C*, 2007, **111**, 404-410.

35. B. Pivovar, F. C. T. Leader, P. Fedkiw, A. R. Mantz and A. B. Pivovar, Alkaline membrane fuel cell workshop final report, 2006.

36. M. Piana, M. Boccia, A. Filpi, E. Flammia, H. A. Miller, M. Orsini, F. Salusti, S. Santiccioli, F. Ciardelli and A. Pucci, *J Power Sources*, 2010, **195**, 5875-5881.

37. L. Zeng and T. S. Zhao, *Electrochem Commun*, 2013, **34**, 278-281.

38. S. Gu, J. Skovgard and Y. S. Yan, *Chemsuschem*, 2012, **5**, 843-848.

39. D. S. Kim, C. H. Fujimoto, M. R. Hibbs, A. Labouriau, Y.-K. Choe and Y. S. Kim, *Macromolecules*, 2013, **46**, 7826-7833.

TOC Graphic
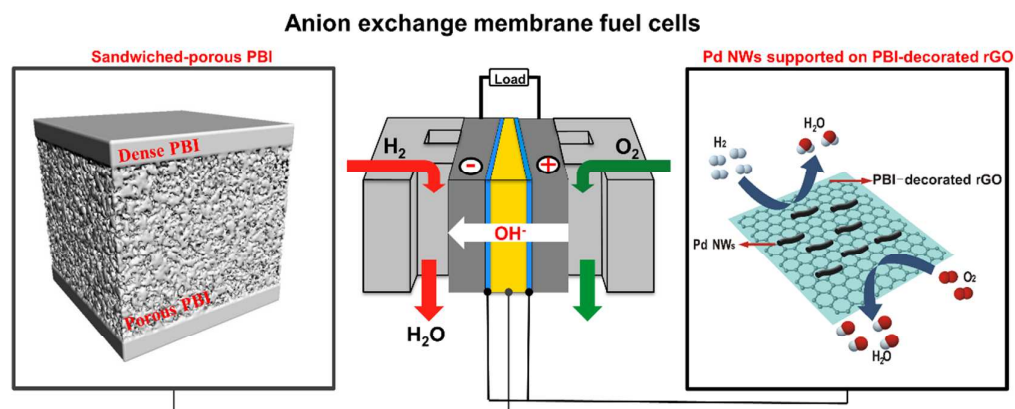
A polybenzimidazole-based membrane electrode assemblies (MEAs) are fabricated with a sandwiched-porous polybenzimidazole (PBI) as the membrane and a new catalyst structure using PBI-decorated reduced graphene oxide as the supporting material. It is demonstrated that the use of new PBI-based MEAs in the anion exchange membrane fuel cell can reach a peak power density of 544 mW cm^{-2} with an improved durability.